

PAPER

Suspension bath bioprinting and maturation of anisotropic meniscal constructs

To cite this article: Margaret E Prendergast et al 2023 Biofabrication 15 035003

View the article online for updates and enhancements.

You may also like

- A biofabrication method to align cells within bioprinted photocrosslinkable and cell-degradable hydrogel constructs via embedded fibers
Margaret E Prendergast, Matthew D

Davidson and Jason A Burdick

- Biofabrication of cell-free dual drugreleasing biomimetic scaffolds for meniscal regeneration Li Hao, Zhao Tianyuan, Yang Zhen et al.

- Effectiveness and biocompatibility of a novel biological adhesive application for repair of meniscal tear on the avascular

zone Takahito Inoue, Tetsushi Taguchi, Shinji Imade et al.

Biofabrication



RECEIVED

2 December 2022

REVISED

22 February 2023

ACCEPTED FOR PUBLICATION 13 March 2023

PUBLISHED 12 April 2023

PAPER

Suspension bath bioprinting and maturation of anisotropic meniscal constructs

Margaret E Prendergast 1 , Su-Jin Heo 1,23, Robert L Mauck 1,23 , and Jason A Burdick 1,4,5,*

- Department of Bioengineering, University of Pennsylvania, Philadelphia, PA 19104, United States of America
- ² McKay Orthopaedic Research Laboratory, Department of Orthopaedic Surgery, Perelman School of Medicine, University of Pennsylvania, Philadelphia, PA, United States of America
- ³ Translational Musculoskeletal Research Center, Corporal Michael J. Crescenz VA Medical Center, Philadelphia, PA, United States of America
- ⁴ BioFrontiers Institute, University of Colorado Boulder, Boulder, CO 80303, United States of America
- Department of Chemical and Biological Engineering, College of Engineering and Applied Science, University of Colorado Boulder, Boulder, CO 80303, United States of America
- * Author to whom any correspondence should be addressed.

E-mail: Jason.burdick@colorado.edu

Keywords: hydrogel, bioprinting, fibers, meniscus, alignment Supplementary material for this article is available online

Abstract

Due to limited intrinsic healing capacity of the meniscus, meniscal injuries pose a significant clinical challenge. The most common method for treatment of damaged meniscal tissues, meniscectomy, leads to improper loading within the knee joint, which can increase the risk of osteoarthritis. Thus, there is a clinical need for the development of constructs for meniscal repair that better replicate meniscal tissue organization to improve load distributions and function over time. Advanced three-

dimensional bioprinting technologies such as suspension bath bioprinting provide some key advantages, such as the ability to support the fabrication of complex structures using non-viscous bioinks. In this work, the suspension bath printing process is utilized to print anisotropic constructs with a unique bioink that contains embedded hydrogel fibers that align via shear stresses during printing. Constructs with and without fibers are printed and then cultured for up to 56 d *in vitro* in a custom clamping system. Printed constructs with fibers demonstrate increased cell and collagen alignment, as well as enhanced tensile moduli when compared to constructs printed without fibers. This work advances the use of biofabrication to develop anisotropic constructs that can be utilized for the repair of meniscal tissue.

1. Introduction

The meniscus is a fibrocartilaginous tissue that provides key functions in healthy knee joints, including transmitting loads, increasing congruency, and improving joint stability [1, 2]. The proper function of the meniscus depends on the specific tissue microarchitecture, particularly the organization of collagen fibers. Due to the low vascularity and limited cell proliferation in adult tissues, the meniscus has a poor healing capacity [3–5]. Injury of the meniscus can lead to improper loading in the joint, which increases the risk of osteoarthritis over time [5]. Current treatment methods, such as partial meniscectomy or meniscal allograft transplantation, have

numerous drawbacks. While meniscectomies provide initial symptomatic relief, these procedures result in altered loading in the joint [3, 5]. Meniscal allograft transplantations provide promising outcomes but are limited in the supply of allograft tissue and the potential for disease transmission [5]. Thus, there is a clear need for improved approaches to repair damaged meniscal tissues.

Acellular scaffold-based strategies such as the collagen meniscus implant (CMI) or the Actifit polyurethane scaffold, indicated for use in patients with segmental meniscus defects, have improved cell infiltration, function, and pain relief when compared to partial meniscectomy treatment [6, 7]; however, these treatments are limited by implant shrinkage and

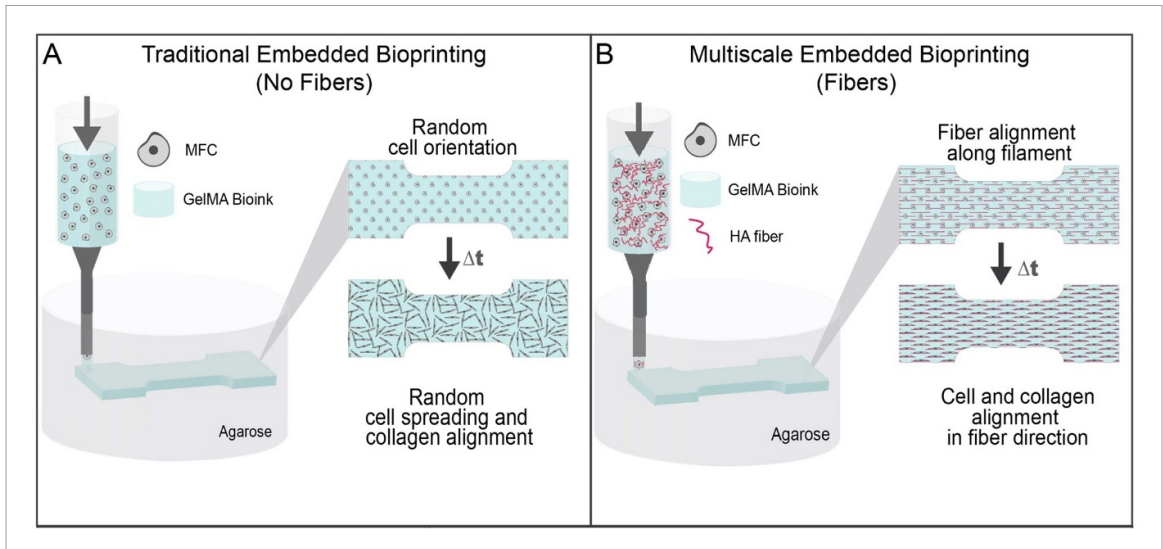


Figure 1. Schematic of embedded bioprinting processes to fabricate meniscal constructs. (A) Traditional embedded bioprinting (denoted 'No Fibers') where a bioink (gelatin methacrylamide (GelMA) with meniscal fibrochondrocytes (MFCs)) is extruded from a printer into an agarose suspension bath and then crosslinked with light. If a cell-degradable material is used as a bioink (e.g. GelMA), cells may degrade the bioink and spread in a random orientation. (B) In our multiscale embedded bioprinting approach (denoted 'Fibers'), microfibers (e.g. crosslinked hyaluronic acid (HA)) within the bioink align in the direction of the printed filament during printing due to shear forces and then are secured in an agarose suspension bath and then crosslinked with light. In this scenario, cell-mediated degradation of the bioink allows spreading, which is guided through the aligned microfibers.

the unorganized matrix deposition that occurs with their use, suggesting decreased mechanical function over time [7, 8]. To improve outcomes, cells have been introduced with the CMI prior to implantation; yet, histological and immunohistochemical analyses still show a disorganized distribution of extracellular matrix (ECM) components, with limited replication of native meniscal architecture [9]. Mimicking this native architecture is key towards restoring the biomechanical function of the meniscus, and as such, other tissue engineering approaches have focused on structurally motivated strategies for meniscal repair [10–13].

Towards this end, electrospun scaffolds of aligned fibers have shown great promise, in which scaffolds of aligned nanofibers provide directional cues to seeded cells for alignment and anisotropic deposition of ECM [10, 14–16]. While this approach has improved matrix organization and overall construct mechanics, limitations include a lack of uniform cell distribution due to issues with cell seeding methods [15-17]. Other methods towards improving matrix organization include mechanical anchoring of cell-laden collagen constructs, which has decreased scaffold shrinkage during culture, and resulted in aligned fiber bundles ranging in 10–350 μ m in diameter and moduli ranging from ~0.04 to 1 MPa after 4 to 6 weeks of culture [18-20]. While these methods offer an exciting advance, the ability to tailor alignment throughout scaffolds is limited and the decoupled tuning of collagen properties can be difficult (e.g. fiber density, pore size and hydrogel stiffness) [21].

Our previous work demonstrates a method to address these concerns, by aligning synthetic fibers with shear forces during extrusion printing to direct cell alignment in three-dimensional (3D) constructs [22, 23]. Modified norbornene-functionalized hyaluronic acid (NorHA) microfibers were fabricated with tunable properties (i.e. degree of modification, lengths) and were embedded in a cell-degradable bioink (gelatin methacrylamide (GelMA)) [22]. GelMA was chosen as a bioink component for its ease of use with bioprinting technologies, its ability to be degraded by cells to allow for spreading, and its capacity for further light-mediated stabilization of the aligned fibers after printing with light [24-27]. HA was chosen for the fabrication of microfibers as it is a common component of the meniscus ECM, it is easily modified, and it provides high cytocompatibility [4, 27, 28]. This study relies on important biofabrication tools, including the suspension bath used for printing, as well as the bioprinting approach used to guide fiber alignment during printing. Bioprinting also allows for the study of various implant sizes and shapes due to the flexibility in the printing process, in this case with cells.

In this current study, this method is now applied to meniscal tissue engineering through the extended culture of meniscal fibrochondrocyte (MFC) laden constructs in a chemically defined chondrogenic medium (figure 1). Over time, the impact of aligned fibers on neo-meniscus formation is assessed through the analysis of cell alignment, matrix content and organization, and bulk construct mechanics. The overall goal of this study is to engineer anisotropic constructs that could be used for the treatment of meniscal tears, rather than the engineering of full meniscal tissues; however, this work provides a step towards these more advanced approaches.

2. Materials and methods

2.1. Material synthesis and NorHA microfiber fabrication

Materials used in this work were either synthesized as previously described or purchased as documented. Synthesis of NorHA was completed as previously described [22, 29]. Briefly, HA was converted to its tetrabutylammonium salt (HA-TBA) through the use of Dowex 50 W proton exchange resin, then frozen and lyophilized. Subsequently, HA-TBA was modified with norbornene groups via esterification with 5-norbornene -2-carboxylic acid (3 equivalent), 4-(dimethylamino)pyridine (1.5 equivalent) and ditert-butyl-decarbonate (0.4 equivalent) for 20 h at 45 °C under nitrogen. Next, the reaction was quenched with water and dialyzed with 0.25 g NaCl/L DiH₂O for 7 d at room temperature. Subsequently, the product was lyophilized. ¹H-NMR (nuclear magnetic resonance) was performed and the degree of modification was determined as 18.8% (figure S1).

Fiber mats were prepared as previously described [22, 23]. Briefly, 3.5 wt% NorHA, 2.5 wt% poly(ethylene oxide) (PEO) (900 kDA), 0.05 (v/v)% 12959, 4 mg ml⁻¹ fluorescein isothiocyanate-dextran (2 MDa) and 0.25 stoichiometric ratio of dithiothreitol to norbornene groups were mixed at 150 rpm for 20 h in deionized (DI) H₂O protected from light. Formulations of 4 wt% PEO (900 kDa) were also mixed in DI H₂O for 20 h. 100 μ l of the PEO formulation was then electrospun onto a strip of aluminum foil on a rotating mandrel (~350 RPM) to create a base layer. Settings of 15%-30% humidity, 28-30 kV applied voltage, 4 kV deflector voltage, ~5 kV collector voltage, 18 cm distance of needle to collector, 18-gauge needle diameter and a 0.7 ml h^{-1} flow rate were used for the PEO formulation. Subsequently, the formulation with NorHA was then loaded and electrospun with the same settings used for the PEO formulation but with a 19 cm distance of needle to collector instead of 18 cm. After electrospinning, fiber mats were immediately crosslinked in a dry state with 10 mW cm⁻² UV light for 2 h under inert nitrogen atmosphere.

Microfibers were fabricated as previously described under aseptic conditions [22, 23]. Briefly, fiber mats were cut into approximately 1 mm³ sections and hydrated for 30 min in phosphate buffered saline (PBS). Next, fibers were repeatedly sheared ($40\times$) with successively smaller needle diameters (18, 21, 23, 30 gauge). Subsequently, solutions were filtered through a 40 μ m cell filter (Falcon® cell strainer, Corning, 352340), followed by a 5 μ m pluristrainer ® (Pluriselect 43-50005-13). Fibers were then again repeatedly sheared ($40\times$) with a 34 gauge needle and then filtered through a 5 μ m pluristrainer ®. After filtration, solutions were centrifuged at 18 000 relative centrifugal force (RCF) and stored at 4 °C for

up to two months, while protected from light. Fibers were imaged with an Olympus BX51 microscope and average fiber lengths were determined through ImageJ software analysis, while fiber concentration was estimated with a hemocytometer.

2.2. Cell isolation

For meniscus fibrochondrocyte (MFC) isolation, medial menisci were harvested from juvenile bovine knee joints (Research 87, 2–3 months old, Boyle, MA). Menisci were cut into approximately 1 mm³ sections, then incubated at 37 °C in Dulbecco's modified eagle's medium (DMEM) with 10% fetal bovine serum (FBS) and 1% P/S over a culture period of 2 weeks to allow cells time to emerge from tissue sections. MFCs at passage 3 or lower were used for all experiments. After expansion, MFCs were trypsinized (0.05%) and resuspended in PBS for use.

2.3. Bioink and suspension bath formulations

GelMA (Allevi by 3D Systems, GMA) was sterilized via germicidal lamp radiation in a laminar flow hood for 30 min prior to dissolving in sterile solutions of PBS. Solutions were heated at 37 °C for 1 h to dissolve GelMA, then photoinitiator (LAP, Colorado Photopolymer Solutions, TPO-Pi), fibers, and cells were mixed into the solution for final concentrations of 5 wt% GelMA, 0.05 wt% LAP, 450×10^6 ml $^{-1}$ fibers and 20×10^6 ml $^{-1}$ cells. The solution was then introduced into a 3 ml syringe (BD, 309657) and loaded into the printer.

Agarose suspension baths were formulated as described previously [30, 31]. Briefly, 0.5 wt% agarose (SeaKem® LE Agarose, VWR 12002-102) was added to DI $\rm H_2O$ and autoclaved at 120 °C for 1 h on a liquid cycle. Directly after autoclaving, the solution was sheared at 700 rpm on a stir plate and allowed to cool to room temperature (25 °C). Solutions were then stored at 4 °C for up to 3 months. Prior to use in bioprinting studies, solutions were diluted to 0.25 wt% with sterile PBS, briefly centrifuged at 500 g for 5 min, and used within 24 h of diluting.

2.4. Viability and fiber, actin, and nuclei orientation analysis

Viability was determined through staining with Hoechst 3342 (Life Technologies H3570) and ethidium homodimer-1 (Thermo Fisher E1169) at 0, 28, and 56 d of culture. Viability was calculated as (total cells — dead cells)/total cells within a single confocal stack. For actin and nuclei imaging, samples were first fixed in 4% formalin, followed by staining of filamentous actin (Alexa fluor 647 phalloidin, thermo fisher) and nuclei were labeled. Confocal images of samples (Leica SP5) were then taken and assessed with ImageJ software. For fiber, actin and nuclei organization, confocal stacks were analyzed with a modified python version of FiberFit software. For

all quantification of confocal images, $n \ge 3$ distinct biological samples were used.

2.5. Fabrication of clamping system for 3D cultures

Clamping system designs were created in Solidworks (figure 2, video S1, file S2–S5). Systems were designed to provide mechanical anchoring of constructs to minimize construct contraction and folding during culture. Designs were exported as STL files and loaded on a Lumen Alpha DLP bioprinter (Volumetric Inc. by 3D Systems). Poly(ethylene glycol) diacrylate (PEGDA) Start Photoink (Cellink, D1611002260) was dispensed into the polydimethylsiloxane (PDMS) vat (Cellink, D16110020872) and processed using crosslink settings suggested by the ink manufacturer (20 mW cm⁻² intensity, 100 μ m layer height, 2 s exposure time, 3×1 st layer time scale factor). After printing was finished, constructs were carefully removed from the build platform with a spatula (18001017, smartSpatula® 210 mm, Fisher Scientific) and washed with PBS to remove the uncured resin. All printing was completed under aseptic conditions. Clamps were stored in sterile containers with PBS at room temperature and used within two weeks of fabrication. Prior to use in culture studies, clamps were briefly washed in 70% ethanol and then three times in sterile PBS.

2.6. Printing and culture of 3D constructs

Print designs were created in SolidWorks (files S5–S6). Designs were exported and uploaded to Repetier Host to create G-code files via Slic3r. Custom modifications to files were made for unidirectional fiber deposition over multiple layers. These files were then loaded to Allevi by 3D systems bioprinting software for printing. Syringes and bioinks were placed in an Allevi 2 bioprinter (Allevi by 3D Systems) with custom fittings for 3 ml syringes to minimize dead space (fittings printed by University of Pennsylvania Libraries' Biotech Commons). All prints were completed at extruder temperatures of 25 °C under aseptic conditions.

After constructs were printed into baths, they were exposed to 10 mW cm⁻² blue light (400-500 nm, Omnicure lamp) for 5 min. Immediately after crosslinking, constructs were released from agarose suspension baths through a series of washing steps (3× sterile PBS). Subsequently, constructs were gently placed into the bottom divets in culture clamps. Next, the top clamps were slid into place on top of the constructs, and secured with screws (92196A077, 18-8 stainless steel socket head screw, Mcmaster-Carr) that had been previously sterilized by soaking in 70% ethanol. These systems were cultured in 8-well plates with PDMS molds. Constructs were cultured for a period of up to 56 d in a chemically defined serum-free chondrogenic media as previously described (highglucose DMEM, 1% penicillin/streptomycin, 0.1 μ M

dexamethasone, 50 μ g ml⁻¹ ascorbate 2-phosphate, 40 μ g ml⁻¹ L-proline, 100 μ g ml⁻¹ sodium pyruvate, 1.25 mg ml⁻¹ bovine serum albumin, 1% ITS+, 10 ng ml⁻¹ TGF β 3) [32, 33].

2.7. Construct mechanical characterization

To determine the compressive moduli of samples, mechanical testing was conducted on a DMA Q800 (TA Instruments) after 0, 28, and 56 d of culture. Hydrogels were first secured in place via a 0.01 N pre-load, and then were compressed at a rate of 0.5 N min⁻¹. Compressive moduli were calculated at a slope from 10%–20% strain.

For tensile testing, samples were loaded in uniaxial tension (Instron 5542, 5 N load cell, 3 mm min⁻¹). The nominal stress was determined as the force on the deformed construct divided by the cross-sectional area of the undeformed construct. The stretch was defined as the deformed length divided by the undeformed length of the construct. The tensile modulus was calculated as the slope from 10% to 20% strain. The yield point was determined from the divergence of the stress–strain curve from a linear fit ($r \le 0.97$). Resilience was calculated as the integral of the stress–strain curve until the yield point. Constructs commonly fractured at sample grips, limiting the calculation of work of fracture, toughness, and ultimate tensile strength [34].

2.8. Construct biochemical characterization

After 0, 28, and 56 d of culture, sections of constructs were evaluated for biochemical composition. Wet weights of sections were recorded, then samples were frozen at $-80\,^{\circ}\mathrm{C}$ and lyophilized. Subsequently, samples were homogenized with the use of disruption beads (Research Products International disruption beads, chrome steel, 2.3 mm) and then digested in 200 $\mu\mathrm{g}$ ml $^{-1}$ proteinase K with 1 mg ml $^{-1}$ hyaluronidase for 20 h. Dimethylmethylene blue, PicoGreen (Picogreen assay kit, Invitrogen P7589) and hydroxyproline assays (Abcam hydroxyproline assay kit, Abcam, ab222941) were then performed to quantify sulfated glycosaminoglycan (sGAG), DNA, and collagen (COL) contents, respectively.

2.9. Construct histological characterization

Constructs were first fixed in 4% formalin at 4 °C for 24 h, then embedded in paraffin. Embedded samples were sectioned (5 μ m) and stained with Alcian Blue (1%, pH 1.0, 1005A, Newcomer supply) or Picrosirius red (Sirius Red, 0.1% in saturated picric acid, Rowley Biochemical, F-357-2). Quantification of staining intensity was carried out in ImageJ as previously described [35, 36]. Alignment index calculations were calculated as previously described [37]. Briefly, equation (1) was used where θ_m is the direction of filament deposition (defined at 0° in images and histograms) and I is the frequency distribution at a specific angle,

$$AI = \frac{\int_{\theta_m - 20^{\circ}}^{\theta_m + 20^{\circ}} I\partial\theta}{\frac{40^{\circ}}{180^{\circ}} x \int_{-90^{\circ}}^{90^{\circ}} I\partial\theta}.$$
 (1)

2.10. Statistical analysis

Circular statistics were performed with R package 'circular' [38]. Comparisons for circular data were analyzed with either the Watson two-test or the Watson-Wheeler test. All other statistic analyses were performed using GraphPad Prism 9 software. Data are reported as mean \pm standard deviation and $n \ge 3$ unless specified otherwise. Comparisons were analyzed with a one-way analysis of variance (ANOVA) with post hoc testing or two-way ANOVA when comparing effects of multiple independent variables. A Bonferroni correction was used for multiple comparisons with $\alpha=0.05$. For all samples, n.s. = not significant, * p < 0.05, ** p < 0.01, **** p < 0.001.

3. Results and discussion

3.1. Printing and culture of meniscal constructs

MFC-laden GelMA constructs were fabricated either without or with fragmented NorHA microfibers by printing into an agarose suspension bath (figure 1, video S2). Specifically, dogbone-shaped constructs of approximately 15 mm in length were printed either without or with fibers for culture up to 8 weeks (figure 2(Ai)). Microfibers were formulated from a previously described process in which electrospun fiber mats are broken up by repeatedly shearing through needles (figure 2(Aii)). The microfibers were approximately 14 μ m in length, which was repeatable during different fabrication batches (figure 2(Aii)). GelMA was chosen as a bioink because it is cytocompatible, supports cell-mediated degradation, and is easily photocrosslinkable [24, 39]. NorHA was chosen as the material for microfibers as it builds on previously developed methods, can be readily processed through electrospinning and utilizes a simple thiol-ene reaction with a di-thiol crosslinker for crosslinking [35]. Microfiber alignment in the direction of printed filaments was confirmed after printing and photocrosslinking (figure 2(Aii)).

Similar to previously published work with collagen constructs, MFC-laden constructs that were cultured in chondrogenic media supplemented with TGF- β 3 contracted over short-term culture periods (<14 d) (figure S2) [18–20]. This was not acceptable for the maintenance of construct anisotropy; thus, an alternative culture platform was needed. Inspired by previous studies using collagen constructs, a clamping system was designed to provide mechanical anchoring for constructs during culture (figures 2(B) and (C)) [19, 20]. Constructs were cultured with this system as dogbone shapes (figure 3(A)) over a period of 56 d and analyzed at

days 0, 28, and 56 through a range of outcome measurements (figure 3(Bi)). Outcome measures ranged from fiber and cell alignment to biochemical and mechanical evaluation (figure 3(Bi)), in which various portions of scaffolds were used for different sets of analyses (figure 3(Aii)).

During the culture period, constructs transitioned from transparent structures that matched the printing dimensions to those that were opaque with rounded edges (figure 3(Bii)). No significant differences in construct heights, widths, or lengths were observed when comparing samples with or without fibers across various timepoints (0, 28, or 56 d), suggesting that the clamping system provides a successful mechanism to minimize construct contraction over time (figure 3(Biii)). Additionally, no significant differences in construct heights, widths, or lengths were observed when comparing constructs without and with fibers at each respective timepoint, demonstrating that embedded fibers have minimal impact on bulk construct dimensions.

3.2. Fiber and cell alignment during culture of meniscal constructs

As a driving factor of tissue mechanics, ECM organization is of particular importance for the meniscus [3, 4, 40]. In addition to having an impact on factors such as proliferation and differentiation, multiple studies have demonstrated that alignment of cells leads to deposition of aligned ECM components such as collagen [41, 42]. Towards this end, a number of methods have been employed to develop anisotropic scaffolds for cell alignment, including the use of electrochemical, magnetic, microfluidic, cyclic stretching and freeze-drying approaches [43–45]. However, these methods have various drawbacks, including the inability to embed cells during fabrication, requiring the use of post-seeding methods that limits uniformity of cell distribution [43, 46]. These limitations motivate the use of biofabrication that allow for fabrication of constructs with cells directly embedded in hydrogel bioinks. Previous work has demonstrated that biofabrication approaches such as extrusion bioprinting can be used to align embedded fibers to subsequently drive cellular alignment [22, 47, 48]. Here, that approach is further explored towards the development of functional anisotropic meniscal tissue constructs.

Previous work indicates that actin alignment is a driving cytoskeletal component for resultant cell alignment, while nuclear alignment and shape have been linked to functional changes in gene expression that can impact matrix deposition [41, 49]. Towards this end, actin, nuclei, and fiber alignment in constructs with and without fibers were assessed at 0, 28, and 56 d of culture. When assessed immediately after printing (0 d of culture), actin and nuclei in all constructs exhibited random orientation,

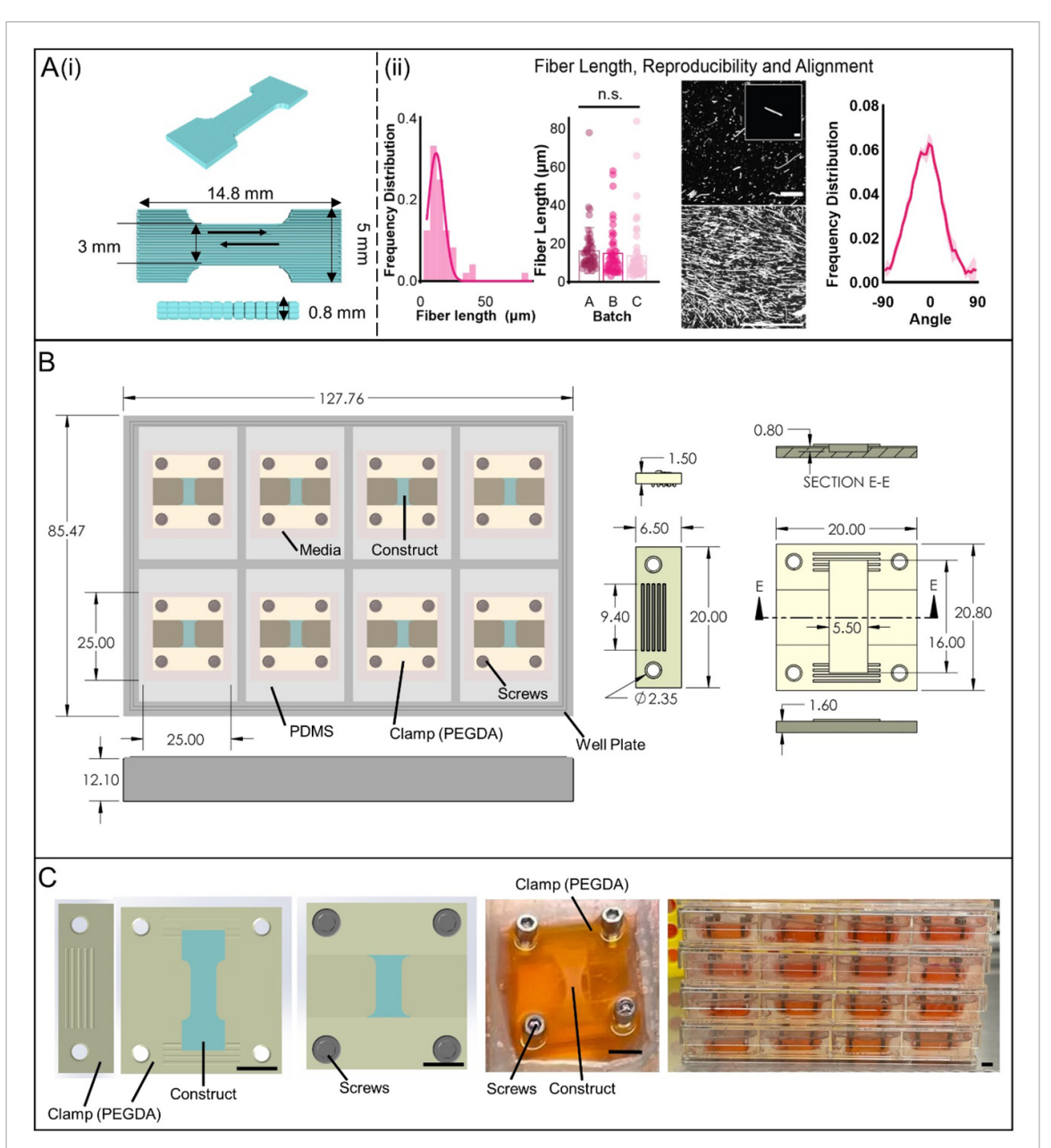


Figure 2. Meniscal construct design. (A) (i) Schematic of printed dogbone constructs (teal, top) and print path with dimensions shown (bottom). Arrows in center designate the direction of filament deposition; (ii) size distribution and batch variability of fragment fibers (left), images of fragmented fibers (middle top, scale bar: 0.1 mm, inset scale bar: 0.01 mm) and aligned fibers after printing (middle bottom, scale bar: 0.1 mm) and quantification of alignment (right) of HA microfibers after embedded printing. (B) Representative schematic of clamping system and well plates used for culture of constructs (units are in mm). (Left) Custom PDMS inserts are placed into 8-well rectangular dishes to create culture dishes with widths and lengths of 25 mm × 25 mm. Constructs are inserted into clamps fabricated on the LumenX with PEGDA Start ink. First, constructs are placed on top of the bottom portion of the clamps, then top pieces of the clamps are slid into place. The assembly is then secured with screws, placed into culture dishes and media is added. (Right) More detailed views of top and bottom clamp pieces are shown with various dimensions. Clamps are designed with grooves so they can be easily slid together, and to further hold constructs in place. Divets at the center of the bottom portion of clamps are designed so constructs can easily slide into place for proper clamping. (C) (Left) Schematic of construct placement in clamps before and after top pieces of clamps are screwed in. (Middle) Representative image of a construct in clamps during culture. (Right) Image of multiple well plates filled with clamped constructs, demonstrating the scalability of the clamping method for culture. Scale bars: 5 mm.

with no significant differences in actin or nuclei alignment between constructs with or without fibers (figure 4). At this same time, fibers demonstrated alignment in the direction of filament deposition, and no significant differences in fiber alignment were found after 28 or 56 d of culture, demonstrating a maintenance of fiber alignment throughout 56 d of culture. At day 28, significant differences in

actin alignment between constructs with and without fibers were observed, while there were still no significant differences in nuclei alignment. By day 56, significant differences in both actin and nuclei alignment between constructs with and without fibers were observed, with increased actin and nuclei alignment observed in constructs with fibers. These results indicated successful alignment of fibers in the

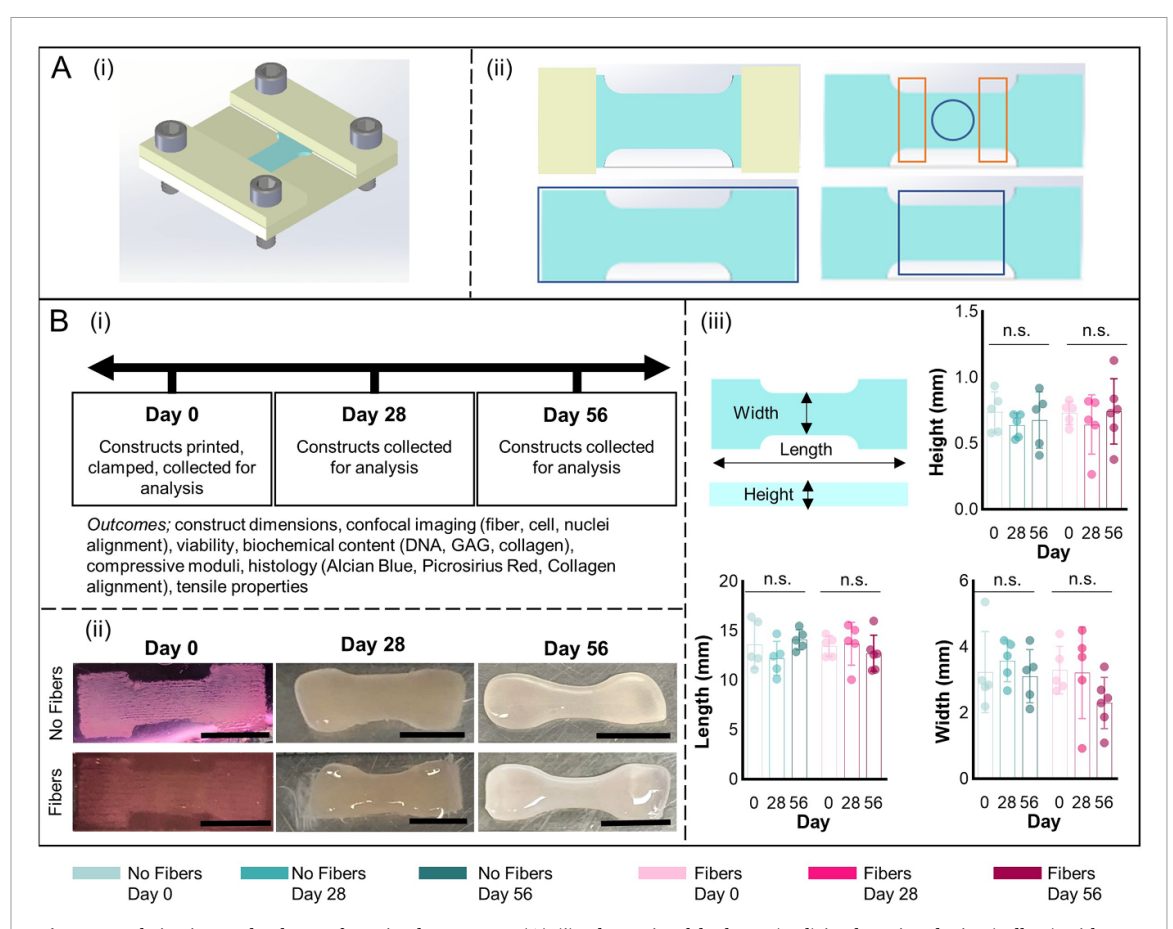


Figure 3. Fabrication and culture of meniscal constructs (A) (i) schematic of dogbone (teal) in clamping device (yellow) with screws (gray) used to secure samples during culture; (ii) schematic of printed dogbone constructs showing (top left) area covered by clamps during culture (yellow), (top right) sections of dogbone used for compressive modulus and viability (black circle) and biochemical assays (orange rectangles), (bottom left) section of dogbone used for tensile testing (black rectangle), (bottom right) section of dogbone used for confocal and histological imaging (black rectangle). (B) (i) Timeline of study design and list of outcome assessments; (ii) images of dogbone constructs fabricated with 'No Fibers' (top) or 'Fibers' (bottom) after 0, 28, and 56 d of culture (scale bars: 5 mm); (iii) schematic of dogbone (teal) and measures of height, length, and width of constructs with 'No Fibers' (teal) or 'Fibers' (pink) after 0, 28 and 56 d of culture. ($n \ge 3$, two-way ANOVA with Bonferroni post hoc, n.s.: no statistical difference).

direction of filament deposition through extrusion printing, and subsequent alignment of cells in the direction of fiber alignment that was maintained through 56 d of culture. These results are in agreement with previous work that soft-embedded hydrogel fibers can be aligned along the direction of filament deposition during extrusion printing, and that this alignment leads to cellular alignment [22, 47, 48].

At 56 d of culture cell alignment was also assessed at various depths through the construct thickness. Actin and nuclei alignment were assessed at approximately 0–0.1 mm distance from the surface (Depth 'A'), 0.2–0.3 mm from the surface (Depth 'B') and 0.4–0.5 mm from the surface (Depth 'C') (figure 5). Fiber alignment was not assessed, as fibers were not visible at Depths A or B. It is possible fibers were not present at these depths for a number of reasons, such as if neotissue had developed at the surface of printed constructs, GelMA in the construct had degraded and fibers had been dislodged from constructs, or if the fluorescein isothiocyanate-dextran had dissipated over time, rendering the fibers invisible

during confocal imaging. While it is likely that some portion of neotissue had developed at the surface of constructs from cell proliferation, it is unlikely that up to 0.3 mm of neotissue had formed on top of the scaffold, as no significant differences in scaffold height were observed from day 0 to day 56 for constructs with or without fibers (figure 3(Biii)). At depth A, constructs with and without fibers demonstrated random actin and nuclei orientation, suggesting random cell spreading at the surface of both constructs. At depths B and C, alignment of actin and nuclei in constructs differed, with increased actin and nuclei alignment observed in constructs with fibers (figure 5). Few other studies of bioprinted anisotropic scaffolds have measured depth-dependent cellular alignment, especially over long culture periods such as for 56 d [47, 48, 50]. At shorter time scales over 7 d, others have reported greater cellular alignment and spreading closer to construct surfaces [50]. Further analysis is needed to fully understand the driving factors behind the depth-dependent cell alignment reported in this work.

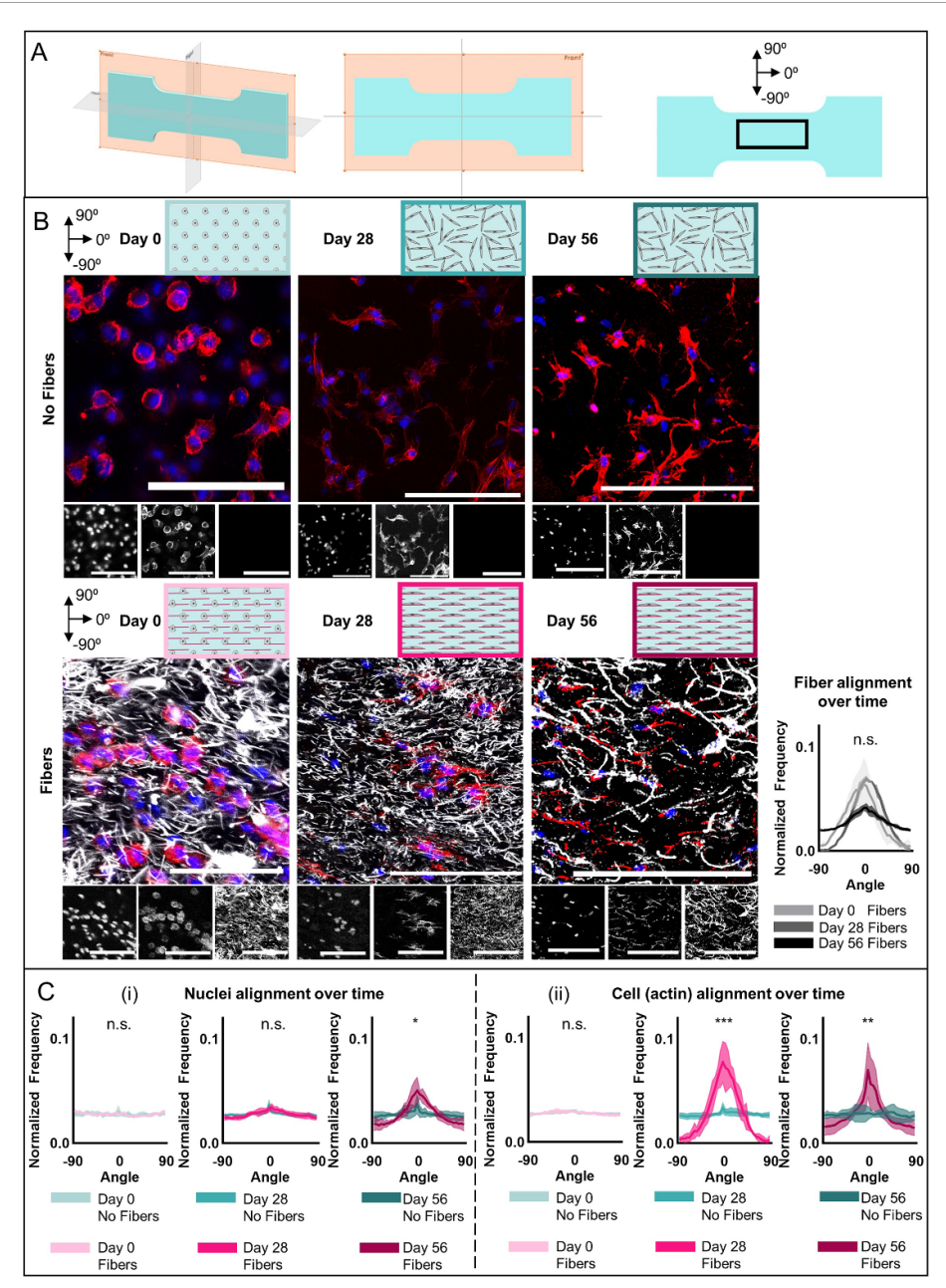


Figure 4. Fiber and cell alignment during culture of meniscal constructs. (A) Schematic of dogbone constructs (teal) showing middle plane (orange) within the samples for confocal imaging (left, middle) and region of constructs imaged denoted by the black bounding box (right). (B) Representative schematics and images of constructs fabricated with 'No Fibers' (top) or 'Fibers' (bottom), cultured for up to 56 d, and stained for MFCs (F-actin: red, cell nuclei: blue) or fibers (gray) (30 μ m z-stacks, scale bars: 0.1 mm). (C) Quantification of (i) nuclei and (ii) actin alignment along the printed filament direction for constructs with 'No Fibers' (teal) or 'Fibers' (pink) after 0, 28, and 56 d of culture. In addition to the differences noted, no statistical differences are observed across 0, 28, and 56 d for No fibers actin (p=0.842) or nuclei (p=0.610) alignment or fibers nuclei (p=0.139) alignment, while p ≤ 0.046 for fibers actin. (n=6 for each group from 3 biologically independent experiments, with two images per biologically independent experiment, mean \pm s.d., Watson test, n.s. = not significant, * $p \leq 0.05$, ** $p \leq 0.01$, *** $p \leq 0.001$).

3.3. Biochemical and mechanical analysis

The viability of MFCs within constructs with and without fibers at 0 d of culture was greater than 90%, demonstrating minimal impact of the printing process on cell viability (figure 6(A)). At 28 d, a drop in viability was seen in constructs with fibers, with significant differences compared to constructs without fibers at day 28 and constructs with fibers at day 0. By day 56, a drop in viability was also

observed in constructs without fibers, with no significant differences in viability between constructs with and without fibers at day 56. While slight decreases in viability were observed, average viability of each group was maintained above 80% at all timepoints, suggesting overall robust viability. Decreased viability over time may be caused by increased matrix deposition, decreasing permeability and nutrient diffusion throughout scaffolds over time [51, 52].

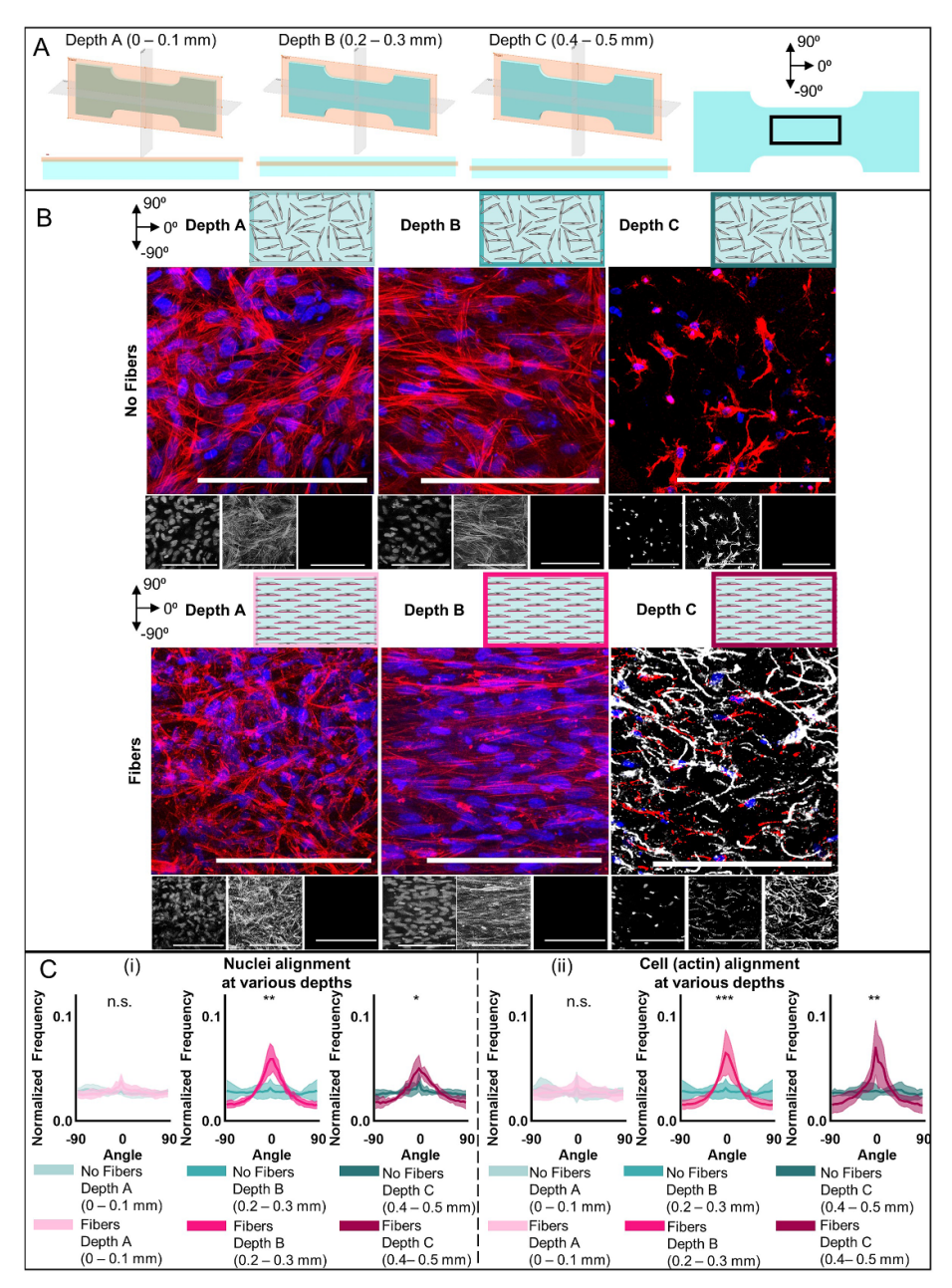


Figure 5. Cell alignment as a function of depth through scaffolds. Cell alignment at various depths after 56 d of culture of meniscal constructs. (A) Schematic of dogbone constructs (teal) showing plane (orange) within the samples at various depths (A: 0–0.1 mm, B: 0.2–0.3 mm, C: 0.4–0.5 mm) for confocal imaging (left) and region of constructs imaged denoted by the black bounding box (right). (B) Representative schematics and images of constructs fabricated with 'No Fibers' (top) or 'Fibers' (bottom), cultured for 56 d, and stained for MFCs (F-actin: red, cell nuclei: blue) or fibers (gray) (30 μ m z-stacks, scale bars: 0.1 mm). (C) Quantification of (i) actin and (ii) nuclei alignment along the printed filament direction for constructs with 'No Fibers' (teal) or 'Fibers' (pink) at various depths. In addition to the differences noted, no statistical differences are observed across various depths A, B, and C for No fibers actin (p=0.956) or nuclei (p=0.825) or for Fibers actin (p=0.068) or nuclei (p=0.133). Note that fibers are not quantified as they were only present within the Depth C group of the Fibers constructs. (n=6 for each group from 3 biologically independent experiments with two images per biological experiment, mean \pm s.d., Watson test, n.s. = not significant, * $p \le 0.05$, ** $p \le 0.01$, *** $p \le 0.001$).

As a first measure of construct maturation, mechanical properties were assessed through dynamic mechanical analysis. Increases in average compressive moduli of printed constructs from 6.9 ± 3.9 kPa and 4.5 ± 1.0 kPa at day $0-218.0\pm76.9$ kPa and 239.7 ± 158.6 kPa at day 56 for constructs were observed without fibers and with fibers, respectively (figure 6(A)). These results demonstrated over 30-fold increases in compressive moduli properties

for all constructs after 56 d of culture. Both constructs with and without fibers reached an average compressive modulus within reported values of native menisci (0.11–0.41 MPa) [53–57]. Even though the compressive moduli of printed constructs at day 0 were much lower than reported values in other meniscal tissue-engineered constructs, compressive moduli at 56 d exceeded values reported in other hydrogel-based systems [12, 58, 59]. These results are consistent

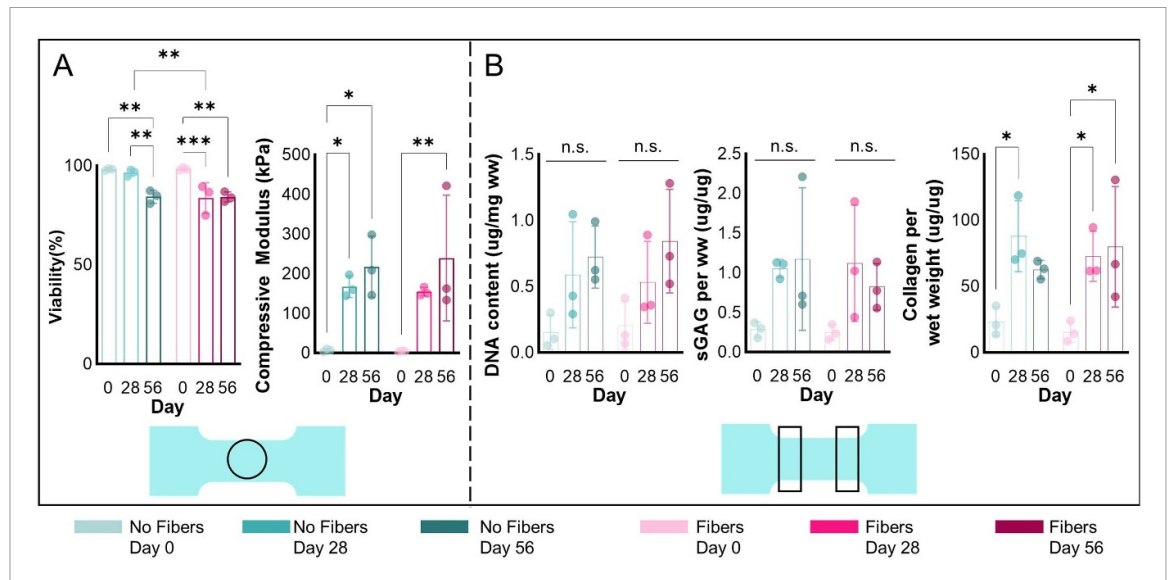


Figure 6. Characterization of viability, compressive modulus, and biochemical content of meniscal constructs during culture. (A) Viability (left) and compressive moduli (right) of constructs fabricated with 'No Fibers' (teal) or 'Fibers' (pink) after 0, 28 and 56 d of culture. (B) DNA content (left), sulfated glycosaminoglycan (sGAG) content (middle), and collagen content (right) of constructs fabricated with 'No Fibers' (teal) or 'Fibers' (pink) after 0, 28 and 56 d of culture. ($n \ge 3$, two-way ANOVA with Bonferroni post hoc, * $p \le 0.05$, ** $p \le 0.01$, *** $p \le 0.001$).

with previous findings that suggest matrix deposition decreases with increasing hydrogel crosslink density, potentially due to increased mesh size in hydrogels with lower crosslink densities [60–62]. Results may suggest an advantage to utilizing synthetically modified hydrogel fibers over collagen-based constructs, where fiber density, pore size, and hydrogel stiffness can be decoupled [17, 21, 23, 62, 63].

Cell proliferation and matrix deposition of collagen and sGAGs, common ECM components found in the meniscus that have been shown to impact tissue mechanics, were assessed after 0, 28 and 56 d of culture [4, 12]. Over 56 d of culture, no significant differences were observed in DNA or sulfated glycosaminoglycan sGAG content normalized to construct wet weight between constructs with and without fibers; however, averages of DNA and sGAG content trended upwards for both groups over time (figure 6(B)). Average DNA content increased more than four-fold from day 0 to day 56 in constructs with and without fibers, while average sGAG content increased more than three-fold from day 0 to day 56 in both constructs with and without fibers. Normalized collagen content in constructs without fibers demonstrated an increase from 0 to 28 d, while collagen content at 28 and 56 d of culture in constructs with fibers demonstrated an increase compared to constructs with fibers at 0 d of culture, with average collagen content increasing more than three-fold in scaffolds with and without fibers over 56 d of culture. No significant differences were observed in DNA, sGAG or collagen content in constructs with or without fibers at each respective timepoint, suggesting that microfibers do not impact proliferation or matrix deposition in constructs. Biochemical content trends

showing time-dependent increases in matrix deposition and cell proliferation supported the increase in compressive moduli observed with dynamic mechanical analysis.

Histological analyses were subsequently used to assess ECM distribution in printed constructs over time (figure 7). Quantification of Alcian Blue staining demonstrated increasing GAG content for scaffolds with and without fibers over 56 d of culture, with a higher average amount of GAGs found in scaffolds without fibers compared to scaffolds with fibers at 56 d of culture (figure 7(B)). Picrosirius red staining was used to assess collagen content and orientation in scaffolds (figures 7(C) and (D)).

Picrosirius red has advantages over other histological methods for assessment of collagen fibers, such as the ability to detect thinner collagen fibers compared to other stains and to provide structural insight when imaged with polarized light microscopy [8, 64, 65]. Brightfield imaging of picrosirius red staining demonstrated variable trends across time in scaffolds with and without fibers under brightfield imaging (figure 7(C)). For constructs without fibers, there was an initial decrease in intensity of picrosirius red staining from day 0 to day 28, then an increase from day 28 to day 56, with no significant differences in stain intensity at day 56 compared to day 0. For constructs with fibers, there were no significant differences in stain intensity from day 0 to day 28, with decreases in stain intensity from day 0 to day 56. These variable results were likely because picrosirius red stains both collagen matrix deposited by cells over time as well as the GelMA bioink, derived from a denatured form of collagen, in constructs [66, 67].

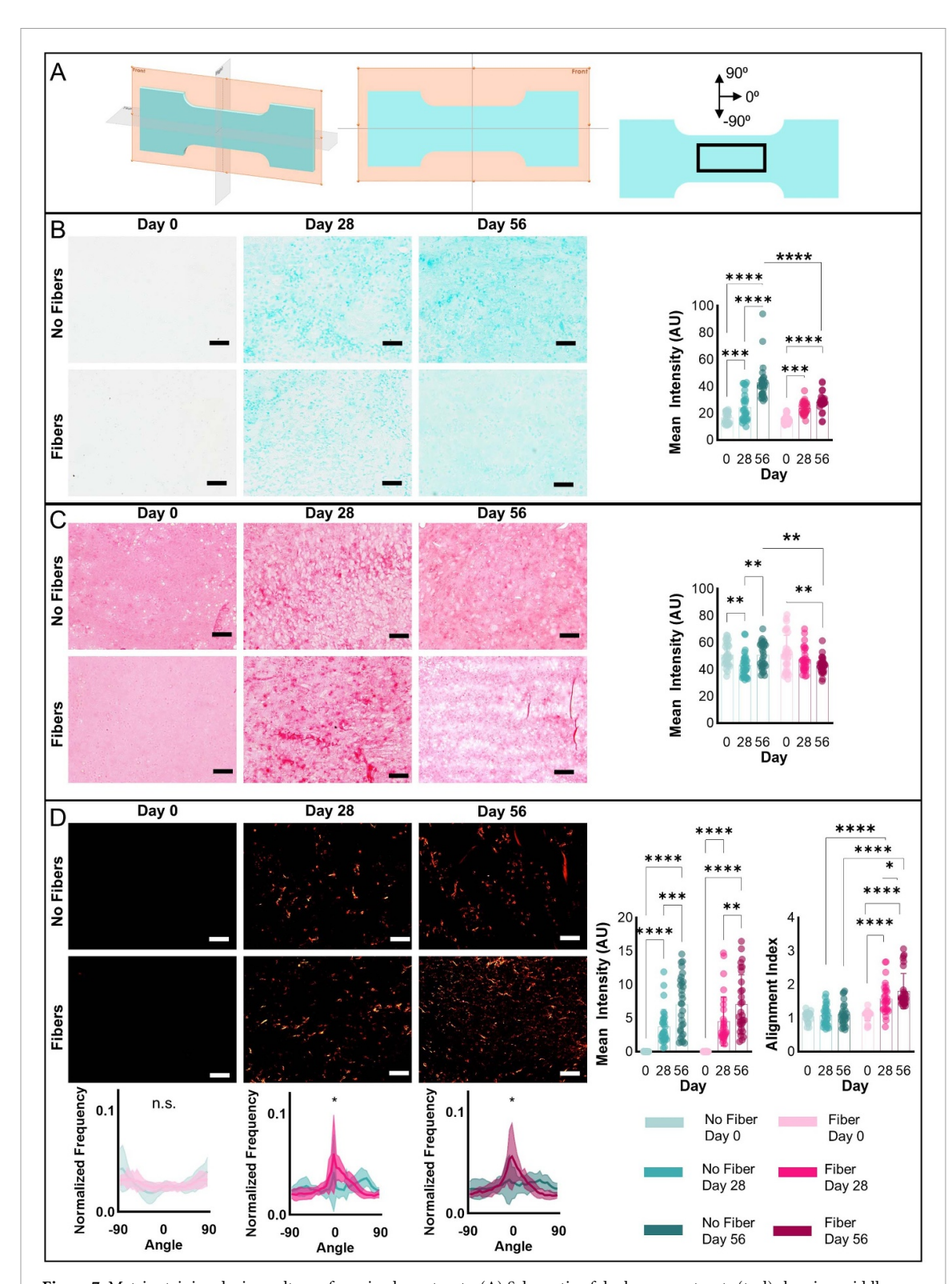


Figure 7. Matrix staining during culture of meniscal constructs. (A) Schematic of dogbone constructs (teal) showing middle plane (orange) sectioned for histology (left, middle) and region of constructs imaged denoted by the black bounding box (right). (B) Representative images and quantification of stain intensity for sGAG via Alcian Blue staining for constructs fabricated with 'No Fibers' (top) or 'Fibers' (bottom) and cultured for 0, 28, or 56 d. Collagen via picrosirius red and imaged under (C) brightfield or (D) polarized light for constructs fabricated with 'No Fibers' (top) or 'Fibers' (bottom) and cultured for 0, 28, or 56 d. Quantification of collagen orientation under polarized light is also shown. (n = 30 images from 3 biologically independent experiments (2 sections per independent experiment, 2–3 images taken per section, scale bars: 0.1 mm), two-way ANOVA with Bonferroni post hoc was used for analysis of stain intensity and alignment index, while Watson test was used for frequency distribution analysis of collagen orientation n.s. = not significant, * $p \le 0.05$, ** $p \le 0.01$, *** $p \le 0.001$ **** $p \le 0.0001$.

Polarized light imaging can be used with picrosirius red staining to differentiate the collagen fiber network in constructs from GelMA content,

in which collagen fibers appear yellow-orange, red or green in color, depending on fiber thickness and packing (figure 7(D)) [68, 69]. Here, clear increases

in overall intensity were noted both in constructs with and without fibers over time. No significant differences were noted between constructs with and without fibers at each specific timepoint, suggesting similar increases in collagen deposition over time. When assessing alignment of collagen in polarized light images by comparing frequency distributions of collagen alignment through circular statistics, no differences between groups were noted at day 0, while an increase in alignment was seen in constructs with fibers compared to constructs without fibers at days 28 and 56. To further assess this alignment, an alignment index, commonly used to assess collagen orientation, was also defined to determine the fraction of collagen fibers aligned within 20° of the angle of interest [12, 70]. This fraction was normalized to the fraction of fibers that would be found within this range if fibers were randomly distributed $(40^{\circ}/180^{\circ} = 0.22)$. Randomly distributed fibers result in alignment indices of 1, while fibers oriented in directions outside the region of interest result in values between 0 and 1, and aligned fibers result in values between 1 and 4.5, with higher values indicating a higher fraction of fibers aligned near the peak angle of interest. Alignment indices in constructs without fibers had no significant differences over time, with average values of 1.06 \pm 0.14, 1.07 \pm 0.29 and 1.11 \pm 0.32 at 0,28 and 56 d, respectively. In contrast, alignment indices in constructs with fibers demonstrated increasing alignment indices over time, with average values of 1.08 \pm 0.15, 1.59 \pm 0.47 and 1.81 ± 0.53 at 0, 28 and 56 d, respectively. Significant differences were observed between alignment indices of constructs with and without fibers at 28 and 56 d, demonstrating higher alignment indices in constructs with fibers.

In addition to assessing staining intensity over time, histological analysis of day 56 samples was also completed at various depths to assess ECM deposition throughout the constructs (figure 8). In constructs without fibers, no differences in the intensity of Alcian Blue stains were observed at various depths assessed (figure 8(B)). However, in constructs with fibers, intensity significantly decreased with increasing depth through the scaffold, suggesting depth-dependent matrix deposition for GAGs in fibrous constructs. Differences between fiber and no fiber groups were seen at more shallow depths (depth A, 0-0.1 mm) and deeper depths (depth C, 0.4–0.5 mm), with more GAGs in fiber groups at Depth A compared to no fiber groups and less GAGs in fiber groups at Depth C compared to no fiber groups. These results may further explain the increased GAG amounts observed in initial histological analysis, which was all performed at deeper depths (depth C, 0.4-0.5 mm). Biochemical analysis suggests that while variations in GAG content were observed between constructs with and without fibers at varying depths, no statistical differences in

bulk GAG content were noted (figure 6(B)). This is supported by results from dynamic mechanical analysis, which also found no statistical differences in compressive moduli between groups at day 56. Previous studies have suggested that the compressive modulus in fibrocartilaginous tissues and constructs is strongly influenced by GAG content of structures [3, 18, 40, 71, 72].

For picrosirius red staining, quantification of brightfield images demonstrated no significant differences in intensity for no fiber groups and varying intensities at different depths for fiber groups (figure 8(C)). Because picrosirius red stains both collagen and GelMA, conclusions about collagen content cannot be determined from analysis of brightfield images alone. Under polarized light images, depth dependent matrix deposition was apparent in constructs with and without fibers, with decreasing collagen content with increasing depth (figure 8(D)). At depth A, a higher intensity of collagen was observed in constructs with fibers compared to constructs without fibers, while no differences at depth B or C were seen between the groups. While both groups exhibit random collagen alignment at depth A close to the surface of scaffolds, constructs with fibers demonstrated increased alignment at depths B and C, following depth-dependent trends observed in cell alignment.

These differences in alignment were apparent when comparing frequency distributions of collagen within constructs as well as alignment index values. Alignment index values demonstrated no differences in collagen alignment across depths for constructs without fibers. In constructs with fibers, higher collagen alignment was observed with increasing matrix depth, with average alignment index values of 1.21 \pm 0.35, 1.61 \pm 0.40 and 1.81 \pm 0.53 for Depths A, B and C, respectively. Additionally, in some select scaffolds with fibers, aligned thicker collagen fibers and bundles were observed at Depth C, while these thicker fibers were not found at this depth in any of the scaffolds without fibers (figure S3). These histological results in figures 7, 8 and S3 suggest that constructs with fibers have the potential to support robust collagen deposition aligned in the direction of printed filaments compared to constructs without fibers. Depth-dependent cell and collagen alignment in constructs with fibers suggest that microfiber alignment, as opposed to organization of ECM matrix at the surface of scaffolds, may drive this alignment. While scaffolds with fibers supported the development of aligned collagen matrix, constructs failed to replicate consistently robust matrix of thicker collagen fibers; however, these results demonstrate that aligned bioprinted microfibers can encourage anisotropic matrix deposition similar to results found in systems such as anisotropic electrospun scaffolds [10, 42]. Future studies may explore enhancing ECM through addition of growth factors

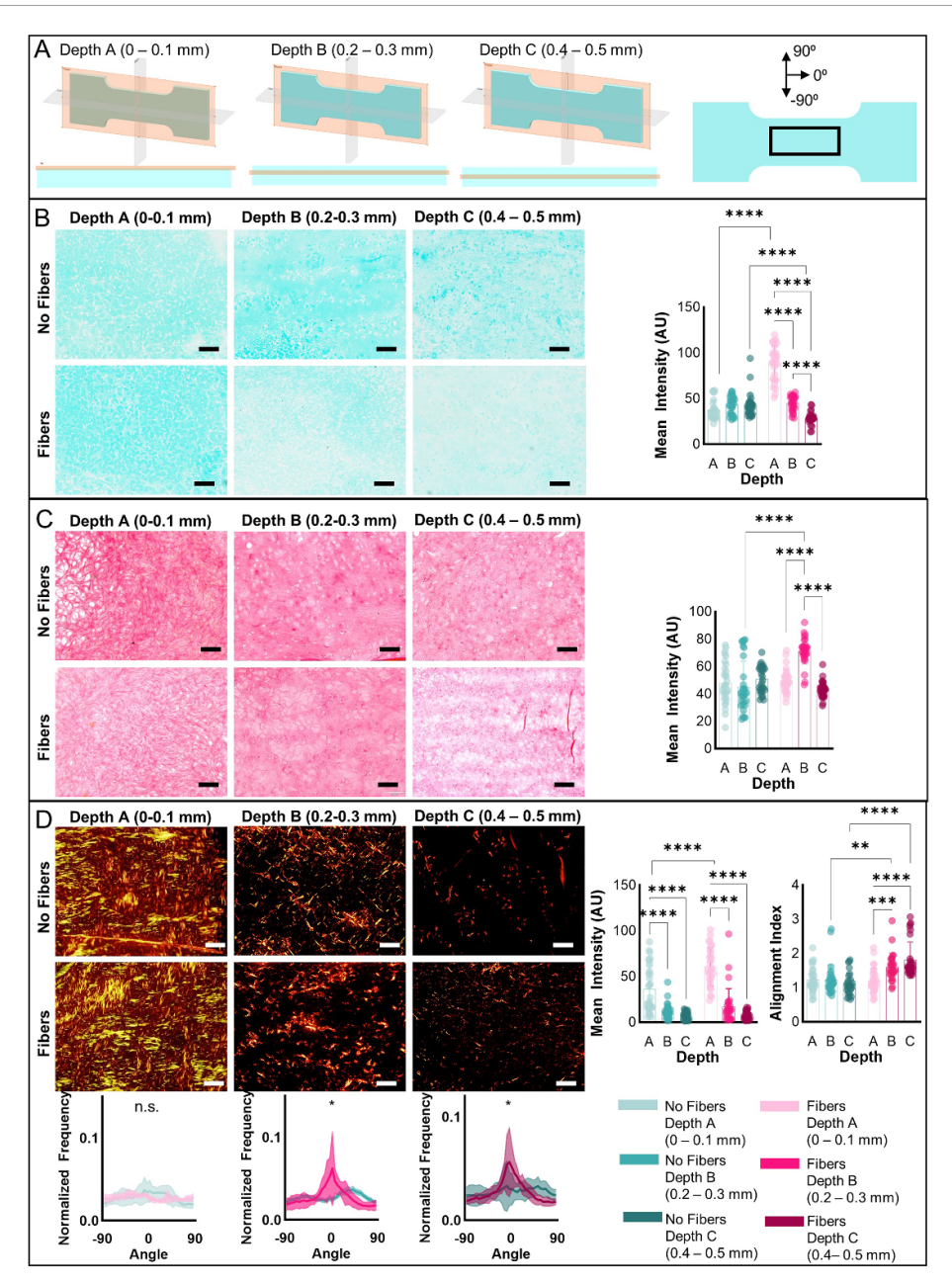


Figure 8. Depth-dependent matrix staining after 56 d of culture of meniscal constructs. (A) Schematic of dogbone constructs (teal) showing plane (orange) within the samples at various depths (A: 0–0.1 mm, B: 0.2–0.3 mm, C: 0.4–0.5 mm) sectioned for histology (left, middle) and region of constructs imaged denoted by the black bounding box (right). (B) Representative images and quantification of stain intensity for sGAG via Alcian Blue staining for constructs fabricated with 'No Fibers' (top) or 'Fibers' (bottom) and cultured for 56 d. Collagen via picrosirius red and imaged under (C) brightfield or (D) polarized light for constructs fabricated with 'No Fibers' (top) or 'Fibers' (bottom) and cultured for 56 d. (n = 30 images from 3 biologically independent experiments (2 sections per independent experiment, 2–3 images taken per section, scale bars: 0.1 mm), two-way ANOVA with Bonferroni post hoc was used for analysis of stain intensity and alignment index, while Watson test was used for frequency distribution analysis of collagen orientation n.s. = not significant, * $p \le 0.05$, ** $p \le 0.01$, *** $p \le 0.001$ *** * $p \le 0.0001$ **.

such as TGF β -1, glucose, or by employing dynamic mechanical loading during culture. Variables such as microfiber stiffness, density and length may also be tuned to assess the impacts of these properties on cell and matrix alignment [18, 73–77].

Depth-dependent matrix deposition demonstrated some disorganization in both scaffolds with and without fibers, but showed a thicker unorganized matrix of collagen and GAGs in scaffolds with fibers compared to those without fibers. It is unclear what

may have caused greater depth-dependence in matrix deposition in scaffolds with fibers compared to those without fibers, but it is likely that permeability of nutrients plays some role in this depth-dependence in matrix deposition [51, 52, 78]. Heterogenous ratios of GAG and collagen content are also observed in native meniscal tissue, and varying GAG concentrations have been shown to impact the development of collagen fibers and overall tissue mechanics in meniscal tissues [18, 74, 79–82]. Future studies may

explore how to leverage the heterogeneity observed in scaffolds, or may employ the use of dynamic culture methods, which have been shown to improve the delivery of nutrients to the center of scaffolds, in order to increase uniformity of matrix deposition throughout scaffolds with fibers [83–87].

Finally, uniaxial tensile testing was performed in the direction of filament deposition and resilience, yield strain, and linear tensile modulus were calculated for constructs with and without fibers after 0, 28, and 56 d of culture (figure 9). At 0 d of culture, constructs exhibited low tensile moduli of 1.6 ± 0.8 and 1.6 ± 1.1 kPa and low resilience values of 0.003 \pm 0.002 and 0.002 \pm 0.002 J m⁻³ for constructs with and without fibers, respectively. While constructs had low tensile moduli, high yield strain values (146.0 \pm 82.0% and 105.0 \pm 42.4% for constructs with and without fibers, respectively) and the linear stress strain curves demonstrated a mechanical response of typical elastic hydrogels [88]. The lack of statistical differences in resilience, yield strain or linear tensile modulus between constructs with and without fibers on day 0 demonstrated that microfibers did not have a significant impact on the initial uniaxial tensile properties of printed constructs.

After 28 d of culture, linear tensile modulus increased significantly in constructs with average values of 650 \pm 252 and 407 \pm 133 kPa for constructs with and without fibers, respectively. Yield strain values also decreased significantly by 28 d of cultures to 20.2 \pm 12.4% and 29.0 \pm 11.7% for constructs with and without fibers, respectively, with no significant differences observed in the resilience of constructs, although average values trended upward. No significant differences in resilience, yield strain or tensile modulus were observed when comparing constructs with and without fibers at 28 d of culture.

By 56 d of culture however, significantly higher average linear tensile moduli of 696 \pm 249 kPa were observed in constructs with fibers compared to average linear tensile moduli of 352 \pm 204 kPa for constructs without fibers. These results demonstrated over 400-fold and over 200-fold increases from average day 0 values for constructs with fibers and without fibers, respectively. While no significant differences were noted in linear tensile moduli from day 28 to day 56 in constructs with or without fibers, a significant increase in resilience was observed in constructs with fibers from day 28 to day 56. Resilience, defined as the integral of the stress-strain curve until the yield point, increases with maturation stage in native menisci and as such an increase in resilience here may suggest further maturation of neomeniscus tissue [84].

Although average tensile moduli did not reach reported ranges observed in native tissue (49–316 MPa in the circumferential direction and 4–71 MPa in the radial direction), increased values

suggested a progression of functional tissue properties over time in both constructs with and without fibers [53, 89]. This result was supported by increases in matrix deposition determined through biochemical and histological analyses. Increased values in linear tensile moduli at 56 d in constructs with fibers compared to constructs without fibers suggest the inclusion of aligned microfibers leads to enhanced biomechanical properties over time in the direction of testing. In previous work, alignment of collagen fibers has been shown to impact mechanics of native tissue and engineered constructs [10, 19, 20, 42, 84]. Therefore, factors such as increased alignment of deposited collagen matrix in constructs with fibers likely played a role in these enhanced mechanics.

It is also possible that the increased amount of unaligned collagen found at Depth A (0–0.1 mm from surface of the scaffold, figure 8) in constructs with fibers compared to constructs without fibers played a role in these different mechanics. However, previous work has suggested that tensile properties such as the linear tensile modulus are more strongly correlated with collagen alignment index and matrix organization compared to overall matrix content, suggesting the differences in collagen alignment in the scaffolds may have been the driving factor for the differences in tensile properties [12, 18, 90]. Additionally, it is unlikely that the differences noted in collagen matrix content based on histological results are large, as biochemical analysis demonstrated no significant differences in overall collagen content between scaffolds with and without fibers at 56 d of culture. Whether surface matrix deposition or collagen alignment at the center of scaffolds drove this change in mechanics, results demonstrated that scaffolds with fibers supported the development of more mechanically robust constructs over time.

3.4. Study limitations and future directions

While the findings show important advances in engineering aligned meniscal tissues, there are limitations to this work. For example, further quantitative analysis of scaffolds could be completed to explore the specific deposited matrix in constructs, such as collagen types or the distribution of components such as decorin, versican and biglycan, which can impact meniscus tissue mechanics and collagen fiber formation [42, 73]. These assessments may help drive directions of future work to further improve upon the matrix organization and mechanics of engineered constructs. While constructs with fibers resulted in matrix development that mimics the native architecture of the meniscus, most constructs did not demonstrate robust collagen fibril development seen in the native meniscus, with mostly smaller aligned collagen fibers observed in fabricated constructs. Additionally, while this fabrication method achieved compressive properties similar to native tissue and enhanced

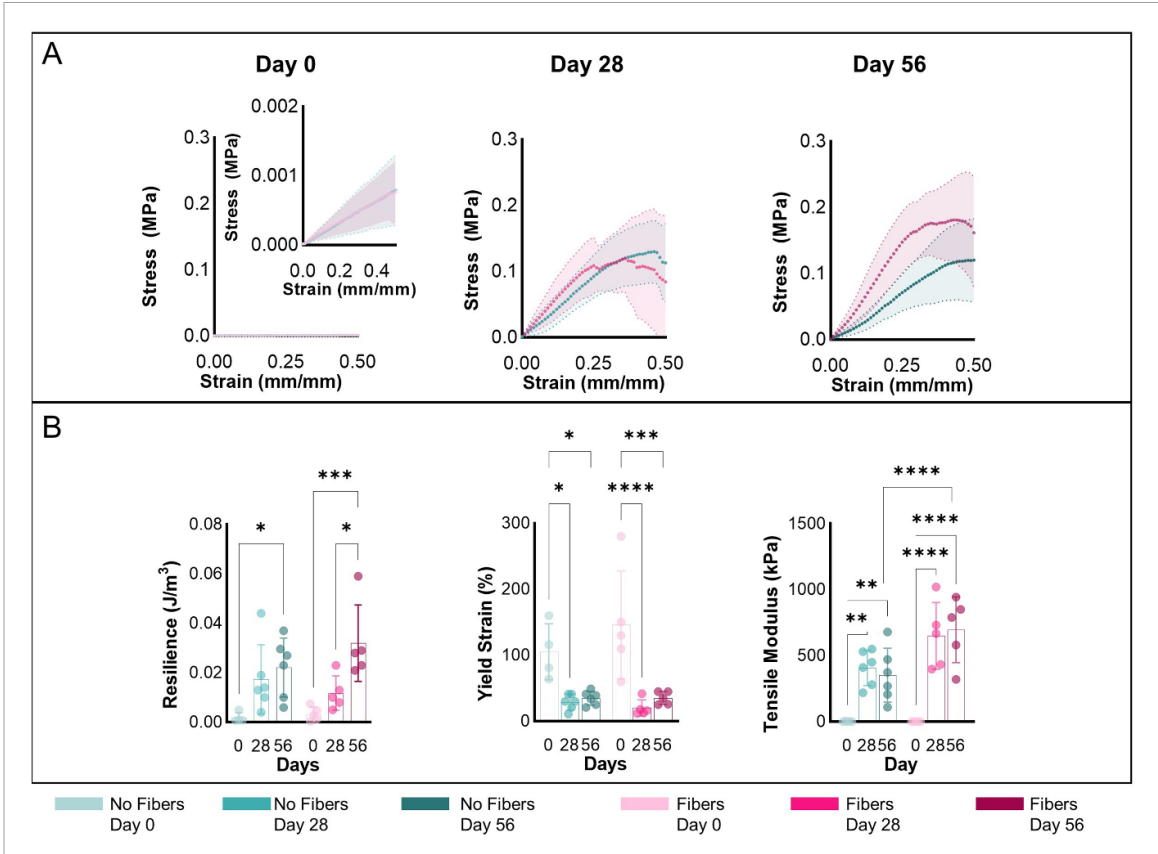


Figure 9. Tensile properties of meniscal constructs during culture. (A) Average stress–strain curves during tensile testing of constructs fabricated with 'No Fibers' (teal) or 'Fibers' (pink) after 0, 28 and 56 d of culture. (B) Resilience (left), yield strain (middle), and tensile modulus (right) of constructs fabricated with 'No Fibers' (teal) or 'Fibers' (pink) after 0, 28 and 56 d of culture. ($n \ge 4$, two-way ANOVA with Bonferroni post hoc, * $p \le 0.05$, ** $p \le 0.01$, *** $p \le 0.001$, *** $p \le 0.001$).

tensile properties over 400-fold from initial construct mechanics, constructs did not reach tensile mechanics within the ranges reported in native tissues. However, these results did demonstrate improvements in matrix organization compared to current methods using acellular collagen sponges, which also have inferior mechanics to native tissue and result in unorganized matrix deposition. As such, results from this study suggest that scaffolds printed with aligned microfibers may provide more robust treatment methods for partial meniscal tears.

Towards further improvement in these scaffold mechanics and microarchitecture, constructs with aligned fibers may be supplemented with other tissue engineering strategies. Meniscus tissue formation is a complex process, and while directional cues for cellular and matrix alignment used in this study enhanced neomeniscus formation, additional biomechanical and biochemical cues are likely needed to encourage more robust tissue development. Future studies may explore additional factors such as glucose and TGF β -1 levels, oxygen levels, and dynamic mechanical cues during culture for further development of neomeniscus formation [12, 18, 37, 73-77, 91, 92]. Alternatively, the inclusion of reinforcing components such as through addition of melt-electrowritten fibers or stronger fibers (e.g. cellulose) may be utilized for the enhancement of bulk construct mechanical

properties [60]. These factors have been proven to impact matrix organization and construct mechanics in previous studies and as such may further bolster results reported in this study towards the development of functional meniscal replacements. Further, our goal was not to engineer an entire meniscus in this study, but steps could be taken to use the principles presented in this study to print larger meniscal constructs that may mimic meniscal tissues, including with radial fibers and varied regions of cartilage composition. However, approaches may need to be taken with larger constructs to address concerns of nutrient transport, such as through the introduction of channels or with culture in bioreactors.

Overall, this work demonstrated the potential for embedded printing of aligned microfibers towards the fabrication of organized tissue engineered meniscal constructs. Future work is needed to assess the engineered meniscal constructs when implanted within meniscal defects, such as in large animal models of meniscal tears, which is outside the scope of this work.

4. Conclusions

This work demonstrated the successful fabrication of constructs with microfiber alignment within printed hydrogel filaments that were maintained for up to 56 d of culture. As reported previously, microfibers embedded in bioinks were aligned in the direction of filament deposition through the leveraging of shear stresses during the biofabrication process. Embedded microfibers did not impact initial construct properties; however, over time, differences in cell alignment between scaffolds with and without fibers were observed, with cells in constructs with aligned microfibers demonstrating alignment in the direction of embedded fibers after 28 and 56 d of culture. Time-dependent differences in construct mechanics and matrix deposition were observed in constructs printed with and without fibers, with increases in matrix deposition, compressive moduli and linear tensile moduli observed. Additionally, an increase in aligned collagen matrix was observed in constructs with fibers after 28 and 56 d of culture, with the formation of thick, aligned collagen fibers observed in select scaffolds with fibers. Finally, a higher average linear tensile modulus was observed in constructs with fibers compared to constructs without fibers at 56 d of culture. These results show the impact of embedded microfibers on neomeniscus formation, demonstrating the potential of this method to fabricate constructs that support neotissue formation with enhanced matrix organization and tissue mechanics. In addition to meniscal tissue engineering, this versatile fabrication technique could also be applied for therapeutic uses in other connective tissues or in biomechanical in vitro studies.

Data availability statement

The data cannot be made publicly available upon publication because no suitable repository exists for hosting data in this field of study. The data that support the findings of this study are available upon reasonable request from the authors.

Acknowledgments

This work was supported by the National Science Foundation through the UPenn MRSEC program (DMR-1720530), the Center for Engineering MechanoBiology STC (CMMI: 15-48571), and a Graduate Research Fellowship (DGE-1845298 to M E P), as well as through the National Institutes of Health (R01 AR056624).

ORCID iDs

Margaret E Prendergast https://orcid.org/0000-0002-2534-5385
Robert L Mauck https://orcid.org/0000-0002-9537-603X
Jason A Burdick https://orcid.org/0000-0002-2006-332X

References

- Greis P E, Bardana D, Holmstrom M C and Burks R T 2002 Meniscal injury: i. Basic science and evaluation *J. Am. Acad. Orthop. Surg.* 10 168–76
- [2] Hasan J, Fisher J and Ingham E 2014 Current strategies in meniscal regeneration J. Biomed. Mater. Res. B 102 619–34
- [3] Makris E A, Hadidi P and Athanasiou K A 2011 The knee meniscus: structure–function, pathophysiology, current repair techniques, and prospects for regeneration *Biomaterials* 32 7411–31
- [4] Fox A J S, Wanivenhaus F, Burge A J, Warren R F and Rodeo S A 2015 The human meniscus: a review of anatomy, function, injury, and advances in treatment *Clin. Anat.* 28 269–87
- [5] Bansal S *et al* 2021 Meniscal repair: the current state and recent advances in augmentation *J. Orthop. Res.* **39** 1368–82
- [6] Buma P, van Tienen T and Veth R 2007 The collagen meniscus implant Expert Rev. Med. Devices 4 507–16
- [7] Tienen T G V, Hannink G and Buma P 2009 Meniscus replacement using synthetic materials Clin. Sports Med. 28 143–56
- [8] Moran C J, Atmaca S, Declercq H A, Cornelissen M J and Verdonk P C 2014 Cell distribution and regenerative activity following meniscus replacement Int. Orthop. 38 1937–44
- [9] Hagmeijer M, Vonk L, Fenu M, van Keep Y, Krych A and Saris D 2019 Meniscus regeneration combining meniscus and mesenchymal stromal cells in a degradable meniscus implant: an in vitro study Eur. Cell Mater. 38 51–62
- [10] Mauck R L and Burdick J A 2015 From repair to regeneration: biomaterials to reprogram the meniscus wound microenvironment Ann. Biomed. Eng. 43 529–42
- [11] Patel J M, Merriam A R, Culp B M, Gatt C J and Dunn M G 2016 One-year outcomes of total meniscus reconstruction using a novel fiber-reinforced scaffold in an ovine model Am. J. Sports Med. 44 898–907
- [12] Puetzer J L and Bonassar L J 2016 Physiologically distributed loading patterns drive the formation of zonally organized collagen structures in tissue-engineered meniscus *Tissue Eng.* A 22 907–16
- [13] Ghodbane S A, Patel J M, Brzezinski A, Lu T M, Gatt C J and Dunn M G 2019 Biomechanical characterization of a novel collagen-hyaluronan infused 3D-printed polymeric device for partial meniscus replacement *J. Biomed. Mater. Res.* B 107 2457–65
- [14] Ionescu L C and Mauck R L 2013 Porosity and cell preseeding influence electrospun scaffold maturation and meniscus integration, in vitro Tissue Eng. A 19 538–47
- [15] Baker B M, Shah R P, Silverstein A M, Esterhai J L, Burdick J A and Mauck R L 2012 Sacrificial nanofibrous composites provide instruction without impediment and enable functional tissue formation *Proc. Natl Acad. Sci.* 109 14176–81
- [16] Mauck R L, Baker B M, Nerurkar N L, Burdick J A, Li W-J, Tuan R S and Elliott D M 2009 Engineering on the straight and narrow: the mechanics of nanofibrous assemblies for fiber-reinforced tissue regeneration *Tissue Eng.* B 15 171–93
- [17] Song K H, Heo S, Peredo A P, Davidson M D, Mauck R L and Burdick J A 2020 Influence of fiber stiffness on meniscal cell migration into dense fibrous networks Adv. Healthc. Mater. 9 1901228
- [18] Kim J, Boys A J, Estroff L A and Bonassar L J 2021 Combining TGF-β1 and mechanical anchoring to enhance collagen fiber formation and alignment in tissue-engineered menisci ACS Biomater. Sci. Eng. 7 1608–20
- [19] Puetzer J L, Koo E and Bonassar L J 2015 Induction of fiber alignment and mechanical anisotropy in tissue engineered menisci with mechanical anchoring *J. Biomech.* 48 1436–43
- [20] Puetzer J L, Ma T, Sallent I, Gelmi A and Stevens M M 2021 Driving hierarchical collagen fiber formation for functional tendon, ligament, and meniscus replacement *Biomaterials* 269 120527

- [21] Matera D L, Wang W Y, Smith M R, Shikanov A and Baker B M 2019 Fiber density modulates cell spreading in 3D interstitial matrix mimetics ACS Biomater. Sci. Eng. 5 2965–75
- [22] Prendergast M E, Davidson M D and Burdick J A 2021 A biofabrication method to align cells within bioprinted photocrosslinkable and cell-degradable hydrogel constructs via embedded fibers *Biofabrication* 13 044108
- [23] Davidson M D, Prendergast M E, Ban E, Xu K L, Mickel G, Mensah P, Dhand A, Janmey P A, Shenoy V B and Burdick J A 2021 Programmable and contractile materials through cell encapsulation in fibrous hydrogel assemblies Sci. Adv. 7 eabi8157
- [24] Yue K, Trujillo-de Santiago G, Alvarez M M, Tamayol A, Annabi N and Khademhosseini A 2015 Synthesis, properties, and biomedical applications of gelatin methacryloyl (GelMA) hydrogels *Biomaterials* 73 254–71
- [25] Liu W et al 2017 Extrusion bioprinting of shear-thinning gelatin methacryloyl bioinks Adv. Healthc. Mater. 6 1601451
- [26] Annabi N, Tamayol A, Uquillas J A, Akbari M, Bertassoni L E, Cha C, Camci-Unal G, Dokmeci M R, Peppas N A and Khademhosseini A 2014 25th anniversary article: rational design and applications of hydrogels in regenerative medicine Adv. Mater. 26 85–124
- [27] Ouyang L, Highley C B, Sun W and Burdick J A 2017 A generalizable strategy for the 3D bioprinting of hydrogels from nonviscous photo-crosslinkable inks Adv. Mater. 29 1604983
- [28] Muir V G and Burdick J A 2020 Chemically modified biopolymers for the formation of biomedical hydrogels Chem. Rev. 121 10908–49
- [29] Gramlich W M, Kim I L and Burdick J A 2013 Synthesis and orthogonal photopatterning of hyaluronic acid hydrogels with thiol-norbornene chemistry *Biomaterials* 34 9803–11
- [30] Senior J J, Cooke M E, Grover L M and Smith A M 2019 Fabrication of complex hydrogel structures using suspended layer additive manufacturing (SLAM) Adv. Funct. Mater. 29 1904845
- [31] Mendes B B, Gómez-Florit M, Hamilton A G, Detamore M S, Domingues R M A, Reis R L and Gomes M E 2019 Human platelet lysate-based nanocomposite bioink for bioprinting hierarchical fibrillar structures *Biofabrication* 12 015012
- [32] Han W M, Heo S-J, Driscoll T P, Delucca J F, McLeod C M, Smith L J, Duncan R L, Mauck R L and Elliott D M 2016 Microstructural heterogeneity directs micromechanics and mechanobiology in native and engineered fibrocartilage Nat. Mater. 15 477–84
- [33] Heo S J et al 2020 Nuclear softening expedites interstitial cell migration in fibrous networks and dense connective tissues Sci. Adv. 6 eaax5083
- [34] Bai R, Yang J and Suo Z 2019 Fatigue of hydrogels Euro. J. Mech. A 74 337–70
- [35] Galarraga J H, Kwon M Y and Burdick J A 2019 3D bioprinting via an *in situ* crosslinking technique towards engineering cartilage tissue *Sci. Rep.* 9 1–12
- [36] Kwon M Y, Vega S L, Gramlich W M, Kim M, Mauck R L and Burdick J A 2018 Dose and timing of N-cadherin mimetic peptides regulate MSC chondrogenesis within hydrogels Adv. Healthc. Mater. 7 1701199
- [37] Setton L A, Guilak F, Hsu E W and Vail T P 1999 Biomechanical factors in tissue engineered meniscal repair Clin. Orthop. Relat. Res. 267 S254–72
- [38] Lund U and Agostinelli C 2017 Package "circular" Repository CRAN pp 1–142
- [39] Lim K S, Galarraga J H, Cui X, Lindberg G C J, Burdick J A and Woodfield T B F 2020 Fundamentals and applications of photo-cross-linking in bioprinting *Chem. Rev.* 120 10662–94
- [40] Melrose J, Smith S, Cake M, Read R and Whitelock J 2005 Comparative spatial and temporal localisation of perlecan, aggrecan and type I, II and IV collagen in the ovine meniscus: an ageing study *Histochem. Cell Biol.* 124 225–35

- [41] Li Y, Huang G, Zhang X, Wang L, Du Y, Lu T J and Xu F 2014 Engineering cell alignment in vitro Biotechnol. Adv. 32 347–65
- [42] Baker B M and Mauck R L 2007 The effect of nanofiber alignment on the maturation of engineered meniscus constructs *Biomaterials* 28 1967–77
- [43] Dewle A, Pathak N, Rakshasmare P and Srivastava A 2020 Multifarious fabrication approaches of producing aligned collagen scaffolds for tissue engineering applications ACS Biomater. Sci. Eng. 6 779–97
- [44] Xing J, Liu N, Xu N, Chen W and Xing D 2022 Engineering complex anisotropic scaffolds beyond simply uniaxial alignment for tissue engineering Adv. Funct. Mater. 32 2110676
- [45] Yang Y, Chen Z, Song X, Zhang Z, Zhang J, Shung K K, Zhou Q and Chen Y 2017 Biomimetic anisotropic reinforcement architectures by electrically assisted nanocomposite 3D printing Adv. Mater. 29 1605750
- [46] de Mori A, Peña Fernández M, Blunn G, Tozzi G and Roldo M 2018 3D printing and electrospinning of composite hydrogels for cartilage and bone tissue engineering *Polymers* 10 285–311
- [47] Schwab A, Hélary C, Richards R G, Alini M, Eglin D and D'Este M 2020 Tissue mimetic hyaluronan bioink containing collagen fibers with controlled orientation modulating cell migration and alignment *Mater. Today Bio.* 7 10058–71
- [48] Nerger B A, Brun P-T and Nelson C M 2019 Microextrusion printing cell-laden networks of type I collagen with patterned fiber alignment and geometry Soft Matter 15 5728–38
- [49] McNulty A L and Guilak F 2015 Mechanobiology of the meniscus J. Biomech. 48 1469–78
- [50] Ahrens J H, Uzel S G M, Skylar-Scott M, Mata M M, Lu A, Kroll K T and Lewis J A 2022 Programming cellular alignment in engineered cardiac tissue via bioprinting anisotropic organ building blocks Adv. Mater. 34 2200217
- [51] Lee M K, Rich M H, Baek K, Lee J and Kong H 2015 Bioinspired tuning of hydrogel permeability-rigidity dependency for 3D cell culture Sci. Rep. 5 8948
- [52] Moor L D, Merovci I, Baetens S, Verstraeten J, Kowalska P, Krysko D V, de Vos W H and Declercq H 2018 High-throughput fabrication of vascularized spheroids for bioprinting *Biofabrication* 10 035009
- [53] Masouros S D, McDermott I D, Amis A A and Bull A M J 2008 Biomechanics of the meniscus-meniscal ligament construct of the knee Knee Surg. Sports Traumatol. Arthrosc. 16 1121–32
- [54] Fithian D C, Kelly M A and Mow V C 1990 Material properties and structure-function relationships in the menisci Clin. Orthop. Relat. Res. 252 19–31
- [55] Bursac P, Arnoczky S and York A 2009 Dynamic compressive behavior of human meniscus correlates with its extra-cellular matrix composition *Biorheology* 46 227–37
- [56] Sweigart M A and Athanasiou K A 2001 Toward tissue engineering of the knee meniscus *Tissue Eng.* 7 111–29
- [57] Baker B M 2010 Meniscus tissue engineering with nanofibrous scaffolds *Dissertation* University of Pennsylvania, Philadelphia
- [58] Yan R et al 2019 A collagen-coated sponge silk scaffold for functional meniscus regeneration J. Tissue Eng. Regen. Med. 13 156–73
- [59] Higashioka M M, Chen J A, Hu J C and Athanasiou K A 2014 Building an anisotropic meniscus with zonal variations *Tissue Eng.* A 20 294–302
- [60] Galarraga J H, Locke R C, Witherel C E, Stoeckl B D, Castilho M, Mauck R L, Malda J, Levato R and Burdick J A 2022 Fabrication of MSC-laden composites of hyaluronic acid hydrogels reinforced with MEW scaffolds for cartilage repair *Biofabrication* 14 014106
- [61] Loebel C, Mauck R L and Burdick J A 2019 Local nascent protein deposition and remodelling guide mesenchymal stromal cell mechanosensing and fate in three-dimensional hydrogels Nat. Mater. 18 883–91

- [62] Erickson I E, Huang A H, Sengupta S, Kestle S, Burdick J A and Mauck R L 2009 Macromer density influences mesenchymal stem cell chondrogenesis and maturation in photocrosslinked hyaluronic acid hydrogels Osteoarthr. Cartil. 17 1639–48
- [63] Davidson C D, Jayco D K P, Matera D L, DePalma S J, Hiraki H L, Wang W Y and Baker B M 2020 Myofibroblast activation in synthetic fibrous matrices composed of dextran vinyl sulfone Acta Biomater. 105 78–86
- [64] Lattouf R, Younes R, Lutomski D, Naaman N, Godeau G, Senni K and Changotade S 2014 Picrosirius red staining J. Hist. Cytochem. 62 751–8
- [65] Rich L and Whittaker P 2005 Collagen and picrosirius red staining: a polarized light assessment of fibrillar hue and spatial distribution J. Morpho. Sci. 22 97–104
- [66] Hori A, Utoh R, Yamada M and Seki M 2021 Preparation of microporous hydrogel sponges for 3D perfusion culture of mammalian cells MATEC Web Conf. vol 333 p 07004
- [67] Moor L D, Smet J, Plovyt M, Bekaert B, Vercruysse C, Asadian M, de Geyter N, van Vlierberghe S, Dubruel P and Declercq H 2021 Engineering microvasculature by 3D bioprinting of prevascularized spheroids in photocrosslinkable gelatin *Biofabrication* 13 045021
- [68] Dai W, Zhang L, Yu Y, Yan W, Zhao F, Fan Y, Cao C, Cai Q, Hu X and Ao Y 2022 3D bioprinting of heterogeneous constructs providing tissue-specific microenvironment based on host—guest modulated dynamic hydrogel bioink for osteochondral regeneration Adv. Funct. Mater. 32 2200710
- [69] Kudva A K, Dikina A D, Luyten F P, Alsberg E and Patterson J 2019 Gelatin microspheres releasing transforming growth factor drive in vitro chondrogenesis of human periosteum derived cells in micromass culture Acta Biomater. 90 287–99
- [70] Gilchrist C L, Ruch D S, Little D and Guilak F 2014 Micro-scale and meso-scale architectural cues cooperate and compete to direct aligned tissue formation *Biomaterials* 35 10015–24
- [71] Nakano T, Dodd C M and Scott P G 1997 Glycosaminoglycans and proteoglycans from different zones of the porcine knee meniscus J. Orthop. Res. 15 213–20
- [72] Skaggs D L, Warden W H and Mow V C 1994 Radial tie fibers influence the tensile properties of the bovine medial meniscus J. Orthop. Res. 12 176–85
- [73] Lopez S G and Bonassar L J 2022 The role of SLRPs and large aggregating proteoglycans in collagen fibrillogenesis, extracellular matrix assembly, and mechanical function of fibrocartilage Connect. Tissue Res. 63 269–86
- [74] McCorry M C, Kim J, Springer N L, Sandy J, Plaas A and Bonassar L J 2019 Regulation of proteoglycan production by varying glucose concentrations controls fiber formation in tissue engineered menisci Acta Biomater. 100 173–83
- [75] Liang Y, Idrees E, Andrews S H J, Labib K, Szojka A, Kunze M, Burbank A D, Mulet-Sierra A, Jomha N M and Adesida A B 2017 Plasticity of human meniscus fibrochondrocytes: a study on effects of mitotic divisions and oxygen tension Sci. Rep. 7 12148
- [76] Croutze R, Jomha N, Uludag H and Adesida A 2013 Matrix forming characteristics of inner and outer human meniscus cells on 3D collagen scaffolds under normal and low oxygen tensions BMC. Musculoskelet. Disorders 14 353

- [77] Huey D J, Athanasiou K A and Almarza A 2011 Tension-compression loading with chemical stimulation results in additive increases to functional properties of anatomic meniscal constructs PLoS One 6 e27857
- [78] Hwang C M, Sant S, Masaeli M, Kachouie N N, Zamanian B, Lee S-H and Khademhosseini A 2010 Fabrication of three-dimensional porous cell-laden hydrogel for tissue engineering *Biofabrication* 2 035003
- [79] Oldberg A and Ruoslahti E 1982 Interactions between chondroitin sulfate proteoglycan, fibronectin and collagen *J. Biol. Chem.* 257 4859–63
- [80] Vogel K G and Trotter J A 1987 The effect of proteoglycans on the morphology of collagen fibrils formed in vitro Colagen Relat. Res. 7 105–14
- [81] Scott J E 1988 Proteoglycan-fibrillar collagen interactions Biochem. J. 252 313–23
- [82] Chen S and Birk D E 2013 The regulatory roles of small leucine-rich proteoglycans in extracellular matrix assembly FEBS J. 280 2120–37
- [83] Bansal S, Mandalapu S, Aeppli C, Qu F, Szczesny S E, Mauck R L and Zgonis M H 2017 Mechanical function near defects in an aligned nanofiber composite is preserved by inclusion of disorganized layers: insight into meniscus structure and function Acta Biomater. 56 102–9
- [84] Bansal S, Peloquin J M, Keah N M, O'Reilly O C, Elliott D M, Mauck R L and Zgonis M H 2020 Structure, function, and defect tolerance with maturation of the radial tie fiber network in the knee meniscus J. Orthop. Res. 38 2709–20
- [85] Guo T, Yu L, Lim C G, Goodley A S, Xiao X, Placone J K, Ferlin K M, Nguyen B-N B, Hsieh A H and Fisher J P 2016 Effect of dynamic culture and periodic compression on human mesenchymal stem cell proliferation and chondrogenesis Ann. Biomed. Eng. 44 2103–13
- [86] Nguyen B B, Ko H and Fisher J P 2016 Tunable osteogenic differentiation of hMPCs in tubular perfusion system bioreactor *Biotechnol. Bioeng.* 113 1805–13
- [87] McMurtrey R J 2016 Analytic models of oxygen and nutrient diffusion, metabolism dynamics, and architecture optimization in three-dimensional tissue constructs with applications and insights in cerebral organoids *Tissue Eng.* C 22 221–49
- [88] Zhuang Z, Zhang Y, Sun S, Li Q, Chen K, An C, Wang L, van den Beucken J J and Wang H 2020 Control of matrix stiffness using methacrylate–gelatin hydrogels for a macrophage-mediated inflammatory response ACS Biomater. Sci. Eng. 6 3091–102
- [89] Lechner K, Hull M L and Howell S M 2000 Is the circumferential tensile modulus within a human medial meniscus affected by the test sample location and cross-sectional area? J. Orthop. Res. 18 945–51
- [90] Wu Y, Puperi D S, Grande-Allen K J and West J L 2017 Ascorbic acid promotes extracellular matrix deposition while preserving valve interstitial cell quiescence within 3D hydrogel scaffolds J. Tissue Eng. Regen. Med. 11 1963–73
- [91] Zhang Z-Z et al 2019 Orchestrated biomechanical, structural, and biochemical stimuli for engineering anisotropic meniscus Sci. Trans. Med. 11 1–13
- [92] Chen M et al 2018 Biomechanical stimulus based strategies for meniscus tissue engineering and regeneration *Tissue Eng.* B 24 392–402